Detailed Seismological Observations from the M_L 5.6 Reno Earthquake Sequence—the Largest Induced Seismic Event in Canada

James P. Verdon*[1], Derek Boeckx[2], Amy Fox[3], Fiona Marshall[4], Mehran Pooladi-Darvish[5], and Neil Watson[3]

Abstract

The M_L 5.6 mainshock within the Reno earthquake sequence in northern Alberta represents the largest induced event in Canada and is among the largest such events globally. We use seismological observations from local monitoring arrays deployed 6 days after the mainshock to develop a detailed understanding of the processes that drove the seismicity and relationships with nearby wastewater disposal (WWD) wells. The seismicity maps out a single fault plane located entirely within the crystalline basement. We used reflection seismic datasets to identify fault structures in the sedimentary section, which could have provided pathways for pressure transfer downward to the reactivated fault plane, and mapped a fault extending from the Belloy Formation down to the basement. If extrapolated through the basement, this structure connects to the position on the mainshock fault plane where the seismicity was densest during the early stages of monitoring. Therefore, this structure represents the most likely conduit for downward pressure transfer from WWD. As mapped in the sedimentary section, it extends through the Belloy and Leduc Formations (the two main targets for WWD), and so pressure could have been transferred from WWD in both formations. However, there is statistically significant temporal correlation between the seismicity and operations in a nearby well in the Belloy Formation, whereas there is no temporal correlation with operations in the nearby Leduc well. The existence of temporal correlation and the spatial proximity of the mapped fault to the Belloy well lead us to conclude that the Belloy well has a stronger connection to the Reno induced seismicity.

Cite this article as Verdon, J. P., D. Boeckx, A. Fox, F. Marshall, M. Pooladi-Darvish, and N. Watson (2026). Detailed Seismological Observations from the M_L 5.6 Reno Earthquake Sequence—the Largest Induced Seismic Event in Canada, *Seismol. Res. Lett.* **XX**, 1–17, doi: 10.1785/0220250127.

Supplemental Material

Introduction

Any subsurface industry that perturbs the state of stress in the deep subsurface has the potential to cause the activation of tectonic faults, leading to induced earthquakes. Induced seismicity has affected most types of deep subsurface industry, including conventional oil and gas, hydraulic fracturing for unconventional hydrocarbons, geothermal energy, carbon capture and storage, natural gas storage, and subsurface wastewater disposal (WWD).

Detailed seismological observations of induced seismicity sequences have been used to map the relationships between operational wells (which introduce perturbations into the subsurface) and the faults on which induced events nucleate (e.g., Igonin *et al.*, 2021; Kettlety *et al.*, 2021). The spatial evolution of induced seismicity sequences can be used to make inferences as to the mechanism(s) that drive induced seismicity (e.g., Kettlety *et al.*, 2020).

In many induced seismicity cases, reactivated faults have been observed to pass within very close proximity to injection wells, such that a direct pore pressure communication between the injection well and the fault is by far the most obvious causative mechanism (e.g., Block *et al.*, 2014). However, in other cases, induced seismicity has been observed at significant distances from the responsible wells, either laterally (e.g., Goebel *et al.*, 2017; Igonin *et al.*, 2021) or with significant vertical separation (e.g., Verdon, 2014; Peña-Castro *et al.*, 2020; Wang

1. School of Earth Sciences, University of Bristol, Bristol, United Kingdom, https://orcid.org/0000-0002-8410-2703 (JPV); 2. DAB Energy, Calgary, Canada; 3. Enlighten Geoscience Ltd., Calgary, Canada, https://orcid.org/0000-0003-0212-8916 (NW); 4. 2228260 Alberta Ltd., Calgary, Canada, https://orcid.org/0009-0009-2439-1855 (FM); 5. MPD Reservoir Engineers Ltd., Calgary, Canada, https://orcid.org/0009-0009-8410-9081 (MP-D)

*Corresponding author: James.Verdon@bristol.ac.uk

et al., 2020; Verdecchia et al., 2021). In such cases, detailed investigations that consider the spatiotemporal evolution of the seismicity, the injection operations, and any pre-existing subsurface structures must be undertaken to fully understand the mechanisms that have allowed the transfer of pressure and/or stress perturbations from the injection well to the faults that host induced seismicity.

Mechanisms for pressure or stress transfer that have been invoked to explain the triggering of induced events away from the immediate vicinity of wells include pressure transfer along high permeability fault or fracture corridors (e.g., Igonin et al., 2021); static transfer of poroelastic stresses associated with an inflating reservoir (e.g., Goebel et al., 2017) or the tensile opening of induced fractures (e.g., Kettlety et al., 2020; Igonin et al., 2022); and aseismic slip or stress transfer along faults (e.g., Eyre et al., 2019; Peña-Castro et al., 2020). Developing an improved understanding of the respective roles of these different mechanisms is important to understand how induced seismicity is triggered, and thereby the factors that can serve to increase the potential likelihood of induced seismicity causation. Similarly, a better understanding of the causative mechanisms of induced seismicity can inform operational strategies adopted to mitigate the rates or magnitudes of events within an ongoing sequence.

In this study, we perform a detailed investigation into the Reno seismicity sequence, which is located in Northern Sunrise County, northern Alberta, Canada, approximately 40 km southeast of the town of Peace River. This sequence initiated in 2017 and peaked with an M_L 5.6 earthquake in November 2022. Schultz et al. (2023) studied this sequence and concluded that the events were induced by nearby WWD activities. Salvage et al. (2024) convened a panel of experts who used induced seismicity attribution schemes (Verdon et al., 2019; Foulger et al., 2023) to conclude that the Reno earthquakes were likely induced. If confirmed as induced, the M_L 5.6 mainshock would be the largest such case in Canada, and among the largest induced earthquakes caused by any industrial activity anywhere in the world. However, several different WWD operations, targeting different geological strata at different depths, are ongoing in the vicinity of the sequence. Salvage et al. (2024) did not attempt to discriminate which operations may have caused or contributed to the seismicity (and which did not), and Schultz et al. (2023) downplayed the heavy oil production itself as a cause, but did not attempt to discriminate between the injection wells at different depths.

Schultz et al. (2023) relied on observations from regional seismic arrays with relatively large location uncertainties, which precluded a detailed investigation of the causative mechanisms of the induced seismicity. In this study, we investigate the Reno sequence using detailed seismological observations obtained from local monitoring arrays that were deployed in the area in response to the M_L 5.6 mainshock. In addition, we use reflection seismic data to map pre-existing tectonic structures in the area to analyze the relationships between the observed seismicity and mapped faults. Our analysis sheds light on the mechanisms that have driven the seismicity in the Reno sequence, and the potential roles played by different nearby WWD wells.

In this study, we do not attempt to develop any coupled reservoir or geomechanical models (e.g., Angus et al., 2016) to simulate pressure or stress perturbations generated by the different wells in the area. Although such models can be useful in assessing potential induced seismicity causation, their limitations should also be recognized. Unless pore pressure and geomechanical observations are available against which model outputs can be compared and history-matched (e.g., Verdon et al., 2011), the outputs from such modeling will be strongly predicated on the user's choices of input physics (e.g., the use of a purely elastic model vs. the inclusion of inelastic effects) and of poorly constrained physical parameters (such as the hydraulic properties of faults invoked as pathways for pressure transfer). As such, we consider the development of reservoir or geomechanical simulations to be beyond the scope of this study, where we focus on seismological and geophysical observations and their spatial and temporal relationships with the industrial operations (e.g., Verdon et al., 2019).

The Reno Earthquake Sequence

Local geology and oilfield operations

Figure 1 shows a schematic representation of the geology in the study area. The crystalline Precambrian basement is overlain by a thin, intermittent sequence of Devonian clastics (the Granite Wash Formation), which in turn is overlain by the Frasnian (Upper Devonian) Leduc Formation. In this area, the top of the Leduc is at a depth of approximately 1900 m below surface (1200 meters below sea level [m.b.s.l.], since the ground elevation in this area is approximately 700 m), and it has a thickness of approximately 300 m. The Leduc is a carbonate reef deposit; its thickness and high porosity and permeability mean that the Leduc Formation is a common target for WWD (Samaroo et al., 2023). To the east of this area, the Leduc reef edge transitions to coeval basin-filling deposits in the form of the Ireton Formation, a shale with low permeability. The Leduc Formation is overlain by approximately 1000 m of Lower Palaeozoic succession, including the Winterburn Group, Wabamun Group, Banff Formation, and Shunda Formation. These formations have experienced little oilfield-related activity in this area, though some are exploited as hydrocarbon reservoirs or WWD targets elsewhere in the Western Canada Sedimentary Basin (WCSB).

The Permian Belloy Formation lies at the top of the Palaeozoic succession, at a depth below the surface of around 800 m. It subcrops against the Pre-Cretaceous unconformity, such that it is substantially thinned and even absent in places. It has high porosity and permeability and is also the target of WWD activities (Samaroo et al., 2023), albeit less so than the Leduc in this area, owing to its more limited thickness.

Within the overlying Cretaceous strata, oilfield activities have focused on heavy oil production from the Bluesky Formation, at

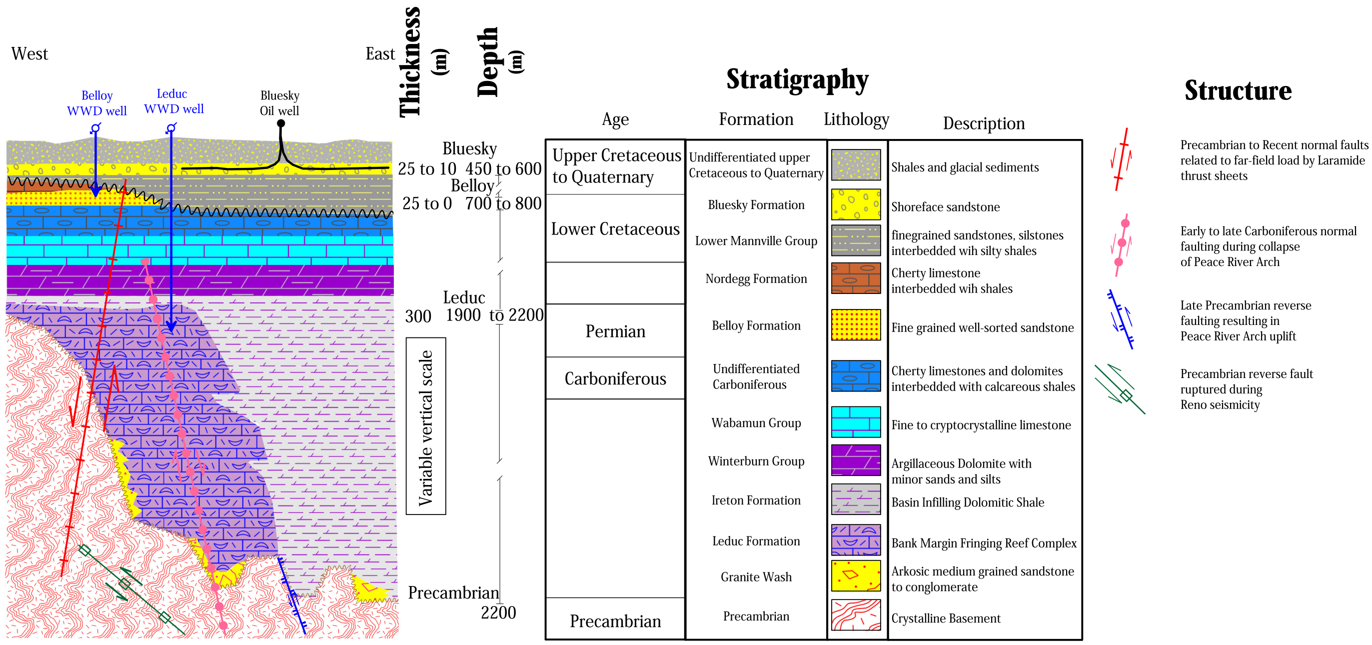

Figure 1. Schematic section showing the geology in the vicinity of the Reno sequence. Wastewater disposal (WWD) takes place in the Leduc and Belloy Formations, and in situ heavy oil extraction takes place in shallow Cretaceous strata. Depths are given below the ground surface, which is at an elevation of approximately 700 m in this area. Note that a variable depth scale is used to highlight key structures at the Leduc and Belloy depths. The color version of this figure is available only in the electronic edition.

depths below the surface of 450–600 m. The coproduced water from this extraction is disposed of into the underlying strata as described earlier. The heavy oil production from Cretaceous strata is thought to be too shallow to be capable of triggering seismicity in the basement (Schultz *et al.*, 2023), and we do not investigate this activity as an induced seismicity cause. There is no hydraulic fracturing taking place in this area.

There are three WWD wells located within the vicinity of the Reno seismicity. The shallowest, Well 100/14-25-082-18W5/00, injects into the Cretaceous-age Peace River Formation. This well is relatively shallow, was injecting relatively low volumes at the time of the 2022 mainshock (Vasyura-Bathke *et al.*, 2023), and is located further to the north (Schultz *et al.*, 2023). These facts mean that it is unlikely to be associated with the Reno seismicity, and we do not consider it further in our study. Well 100/14-18-082-17W5/00 targets the Leduc Formation, and Well 100/06-14-082-18W5/00 targets the Belloy Formation. Hereafter, we refer to these wells as the Leduc Well and the Belloy Well, respectively (see Fig. 2a). Figure 2b shows the monthly injection volumes in these two wells. Note that there are additional disposal wells at greater distances from the Reno sequence (the nearest of which is approximately 15 km from the Reno sequence), most of which target the Leduc Formation. We do not consider these wells in this study, but we recognize that they may have contributed to the pressure change within the Leduc across a wider area (see fig. 1 of Schultz *et al.*, 2023 for the regional context).

Seismicity, monitoring, and regulatory actions

Monitoring in the Reno area was originally provided by regional arrays with relatively sparse station spacing. In Figure 2, we show all earthquakes in the Reno area recorded in the Alberta Earthquake Dashboard (Alberta Geological Survey [AGS], 2020), which uses regional monitoring networks such as the Regional Alberta Observatory for Earthquake Studies Network (RAVEN, see Schultz and Stern, 2015). This catalog begins in 2006. The first events in the Reno sequence were detected in 2017, followed by a small burst of events in 2021. Seismicity accelerated considerably with the M_L 5.6 event on 30 November 2022, and an M_L 5.1 event on 16 March 2023. The large location uncertainties produced by the regional monitoring arrays mean that no clear structures can be discerned from the seismicity "cloud" in Figure 2.

Initially, the Alberta Energy Regulator (AER) stated that the M_L 5.6 event was natural. Nevertheless, the Alberta Geological Survey (AGS) commissioned a local nodal monitoring array to better characterize the sequence—the deployment of this array is described by Gu *et al.* (2025) and referred to as the Peace River Induced Seismic Monitoring (PRISM) array. This array operated from December 2022 to mid-April 2023. The PRISM Array used nodal instruments, which had to be retrieved and replaced at roughly monthly intervals. Hence, the PRISM array data were acquired in three "Rounds," the operational dates of which were: 6 December 2022 to 13 January 2023 (round 1), 26 January 2023 to 3 March 2023 (round 2); 10 March 2023 to 14 April 2023 (round 3). We have available data from eight stations during round 1, and six stations during rounds 2 and 3.

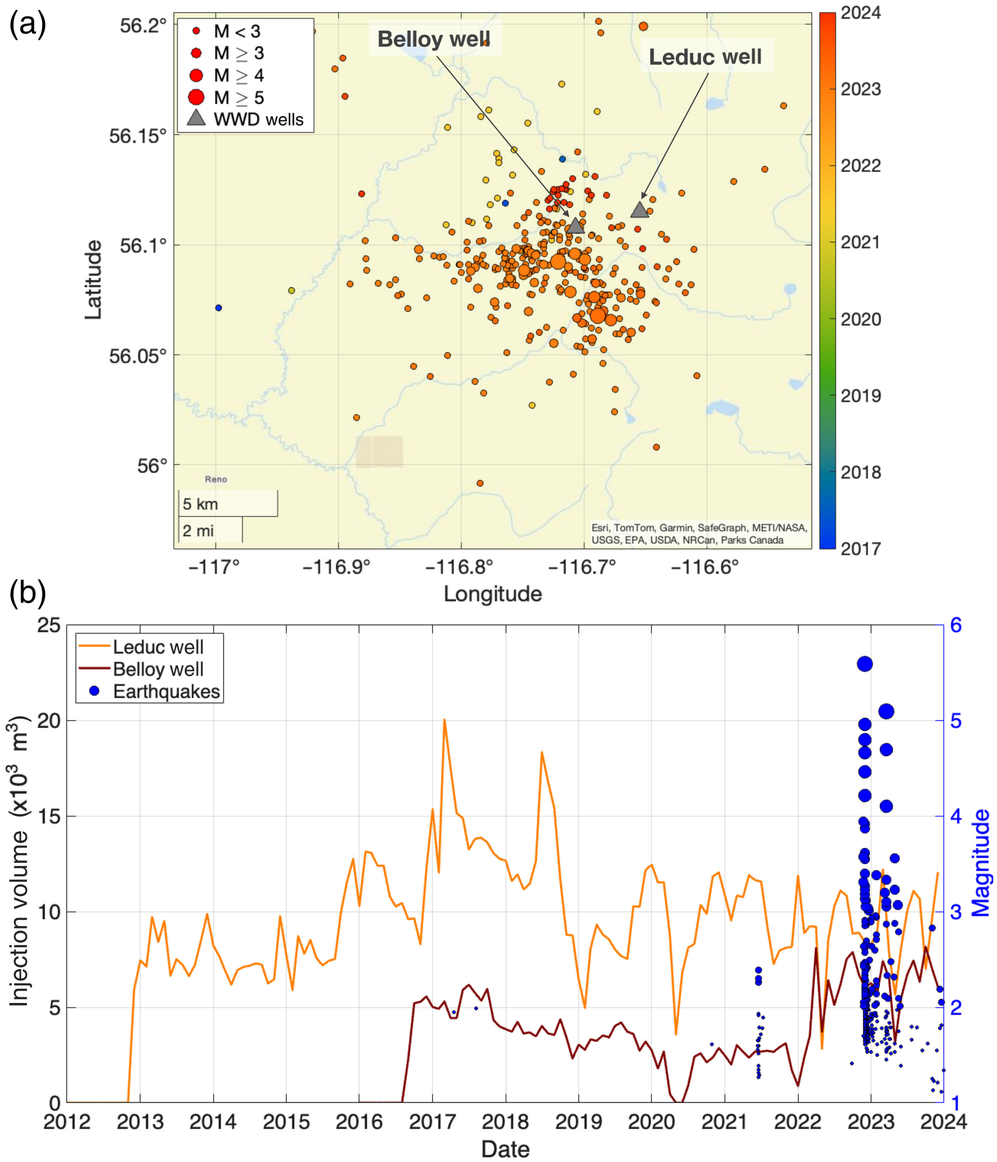

Figure 2. (a) Map and (b) timeline of the Reno seismicity cluster, based on observations from regional earthquake monitoring. In panel (a), events are sized by magnitude and colored by date. The two nearby WWD wells are marked by gray triangles. In panel (b), the monthly injection volumes into the Leduc and Belloy Wells are marked by orange and red lines, respectively. The color version of this figure is available only in the electronic edition.

After the March 2023 M_L 5.1 event, the AER changed its view, determining that the Reno sequence was induced and caused solely by WWD in the Leduc Well (Alberta Energy Regulator [AER], 2023). The operator of this well was mandated by the AER's Environmental Protection Order to install a new local monitoring array. We refer to this array as the operator array. The operator array has been recorded continuously from 10 April 2023 to the present. Our analysis period spans from the deployment of the PRISM array from December 2022 to mid-April 2023, followed by the operator array from April 2023 to February 2024. See the supplemental material (Table ST1 and Fig. SF1) for full details of the monitoring array instrumentation, locations, and monitoring periods.

Earthquake Locations and Magnitudes

Processing methodology

Preliminary event detections were performed by processing contractors commissioned by the AGS and the Leduc Well operator. These preliminary detections form the basis of our dataset. We performed a visual analysis of the waveforms for each reported event to manually pick *P*- and *S*-wave phases. Figure 3 shows example waveforms from a magnitude M_L 0.8 event. We required a minimum number of picks to take an event forward for the location (we varied this threshold depending on the number of stations available in the array, see supplemental material section S1). Our final catalog consists of 881 events, with a magnitude of completeness of $M_c = 0.5$ for the northwest cluster of events and $M_c = 0.6$ for the southeast cluster of events (see Fig. SF6 for an evaluation of detection thresholds).

We developed a *P*-wave velocity model based on compressional-wave well log data from a nearby well (Fig. SF2). Because the *S*-wave velocities were unconstrained, we performed locations using a range of V_P/V_S ratios (from 1.6 to 1.9), selecting the value ($V_P/V_S = 1.85$) that minimized the overall misfit between observed and modeled *P*- and *S*-wave picks (Table ST2 lists the pick residuals for each station). Having defined the velocity model, we inverted our *P*- and *S*-wave picks to find the best-fit locations that minimized the root-mean-squared residuals between modeled and observed arrival times. *P*- and *S*-wave travel times were modeled using an Eikonal solver (Podvin and Lecomte, 1991). We used the Neighborhood Algorithm (Sambridge, 1999) to perform a

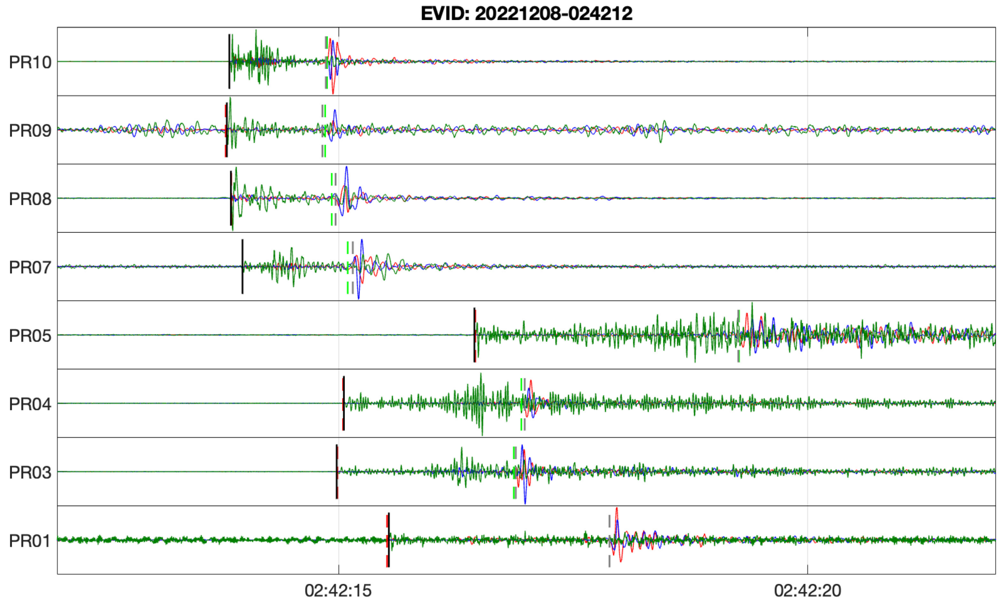

Figure 3. Waveforms from an M_L 0.8 event recorded by the Peace River Induced Seismic Monitoring (PRISM) array. Traces show vertical (green), north–south (red), and east–west (blue) components. Solid black and green dashed lines show the manual *P*- and *S*-wave picks, respectively. Red and gray dashed lines show the modeled *P*- and *S*-wave arrival times from the best-fit hypocentral location. We find an excellent match with low residuals between observed and modeled arrival times. The color version of this figure is available only in the electronic edition.

global minimization for the best-fitting event locations that minimize travel-time residuals. Our location uncertainties are typically within ±200 m laterally, and ±250 m vertically (see Figs. SF3 and SF4 for uncertainty assessments). There was a brief period in April 2023 when both the PRISM and operator arrays were active. In our supplemental material (Fig. SF5), we compare the locations of events detected by both arrays, finding that the locations using each array were consistent.

We used the local scale of Yenier (2017) to compute local magnitudes. Note that the gain settings on the PRISM array instruments were set such that the waveforms for events with magnitudes greater than approximately M_L 3.1 were clipped. For the clipped events, we adopted the magnitudes reported by the Alberta Earthquake Dashboard (AGS, 2020) from regional monitoring arrays.

Results

Our earthquake locations are plotted in Figure 4, and a timeline of seismicity is provided in Figure 5. A 3D electronic figure showing the event locations, the injection wells, and other structural features is provided in Figure ESF1, along with the event catalog (Table EST1). The event locations provide a detailed view of the fault on which the Reno sequence occurred. The overwhelming majority of events are well fitted by a single planar structure that is located at depths of 3700–7000 m below surface (3000–6300 m.b.s.l.). The top of the crystalline basement is at approximately 2100–2200 m below surface (1300–1500 m.b.s.l.), so the located events are all within the crystalline basement (even accounting for the hypocenter location uncertainties).

The plane in Figure 4 shows the plane of the least-squares fit to the observed locations. This plane has a strike of 300° and a dip of 43°, a length along strike of approximately 8 km, and a width down-dip of approximately 4 km. The highest density of events is focused at the northwestern corner of this plane, at the up-dip edge. Schultz *et al.* (2023) and Vasyura-Bathke *et al.* (2023) have both computed source mechanisms for the M_L 5.6 mainshock event, using a combination of regional seismic observations and Interferometric Synthetic Aperture Radar (InSAR) ground deformation measurements. Vasyura-Bathke placed events at depths of between 3 and 7 km below the surface (based on Fig. 4 therein), and Schultz *et al.* (2023) placed most events between 2 and 7 km below the surface. Both studies produced a reverse fault focal mechanism for the M_L 5.6 mainshock, with slip occurring on a plane with a northwest–southeast strike, dipping to the northeast. The orientation and position of the fault plane mapped by our event locations (Fig. 4) is consistent with the Schultz *et al.* (2023) and Vasyura-Bathke *et al.* (2023) mainshock focal mechanism estimates. Gu *et al.* (2025) computed focal mechanisms using data from the PRISM array, also finding that the majority of events have reverse faulting mechanisms with northwest–southeast strikes.

The azimuth of the maximum horizontal stress $S_{H\,max}$ in this area is northeast–southwest (Bell *et al.*, 1994). Stress estimates based on well breakouts and well tests in the area indicate that stress conditions are strike-slip within the Leduc Formation (based on proprietary industry data). Therefore, the observed reverse faulting is inconsistent with stress conditions observed within the sedimentary strata. Lund Snee and Zoback (2020) developed a stress map for North America primarily based on earthquake observations. Because earthquakes occur predominantly in basement rocks, the Lund Snee and Zoback (2020) stress map can be taken as mapping stress conditions in the crystalline basement. In this area, Lund Snee and Zoback (2020) gave a stress regime that is transitional between strike-slip and reverse (with $S_{H\,max}$ still orientated northeast–southwest). This transition

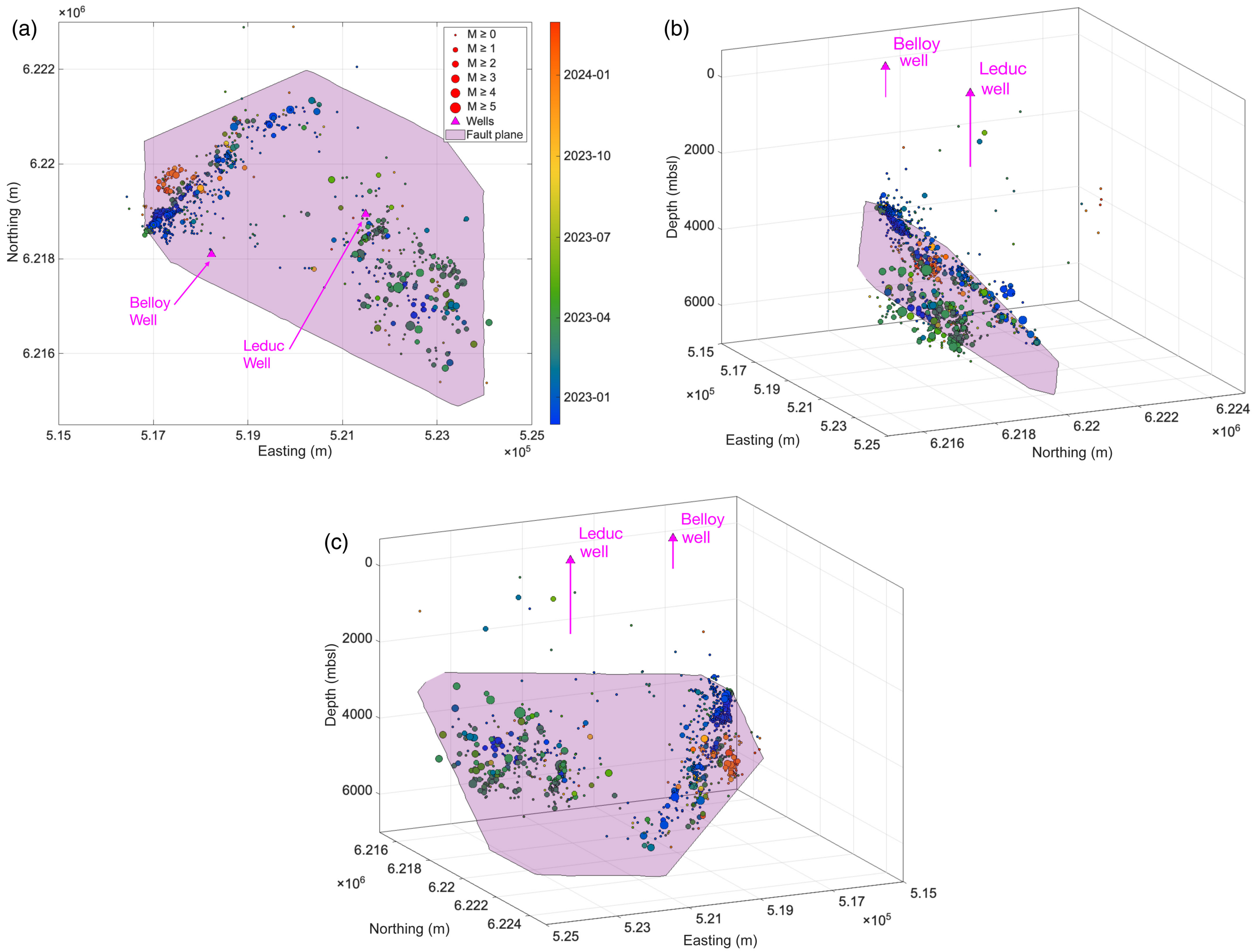

in stress conditions, from strike-slip within the sediments to reverse within the basement, is easily explained by an increase in maximum horizontal stress in the basement relative to the sediments. This effect would be consistent with theoretical considerations of how the different mechanical properties of sediments versus basement rocks would affect the resulting stress conditions (e.g., Vilarrasa and Carrera, 2015).

The reverse faulting focal mechanisms observed by Schultz *et al.* (2023), Vasyura-Bathke *et al.* (2023), and Gu *et al.* (2025) are therefore consistent with stress conditions estimated for the underlying basement, but are not consistent with the strike-slip stress conditions observed in the sediments. Hence, the focal mechanisms provide an independent constraint for the depth of faulting because they indicate that fault ruptures are occurring within the basement, not the sediments. We would expect to have observed strike-slip faulting on structures oriented approximately 30° from $S_{H\max}$ if ruptures were occurring within the sediments, where stress conditions are strike-slip.

The size of the mapped fault plane, with a total area of approximately 30 km^2, is consistent with the dimensions of rupture necessary to host an M_L 5.6 event (roughly 5–80 km^2, based on typical fault scaling relationships, see Nantanoi *et al.*, 2022). Since the M_L 5.6 mainshock occurred before the installation of local arrays, its hypocentral location has a larger uncertainty. However, given the consistency of the mapped plane with the mainshock focal mechanism and the match in terms of rupture area, we are confident that the fault plane mapped by the aftershocks delineates the position of the mainshock rupture. We refer to this feature as the "mainshock fault plane", or MFP, hereafter.

Figure 4. (a) Map view and (b,c) 3D views of the seismicity recorded by the local arrays deployed in response to the M_L 5.6 mainshock. Lateral coordinates are UTM. Events are colored by occurrence date and sized by magnitude. The two nearby wells (the Leduc and Belloy Wells) are marked with pink triangles showing the well pads and vertical lines showing the well depths. The purple patch shows the best-fit plane running through the event hypocenters. Depths are given in meters below sea level (m.b.s.l.). The color version of this figure is available only in the electronic edition.

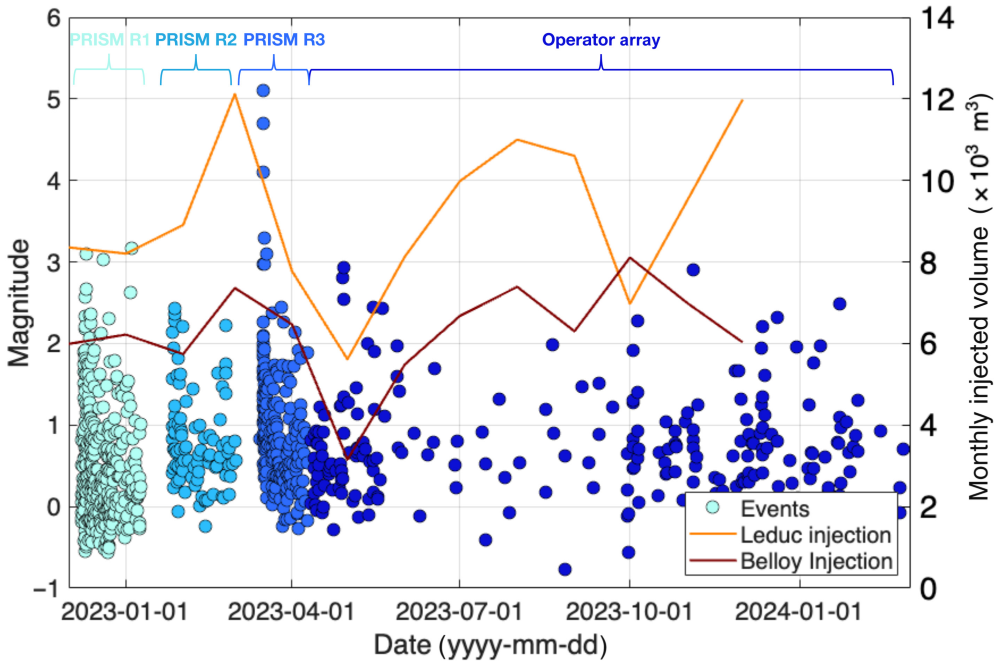

Figure 5. Timeline of seismicity recorded by the local monitoring arrays: events are colored by the array recording periods. We also show the monthly injection volumes in the Leduc (orange) and Belloy (red) wells. The color version of this figure is available only in the electronic edition.

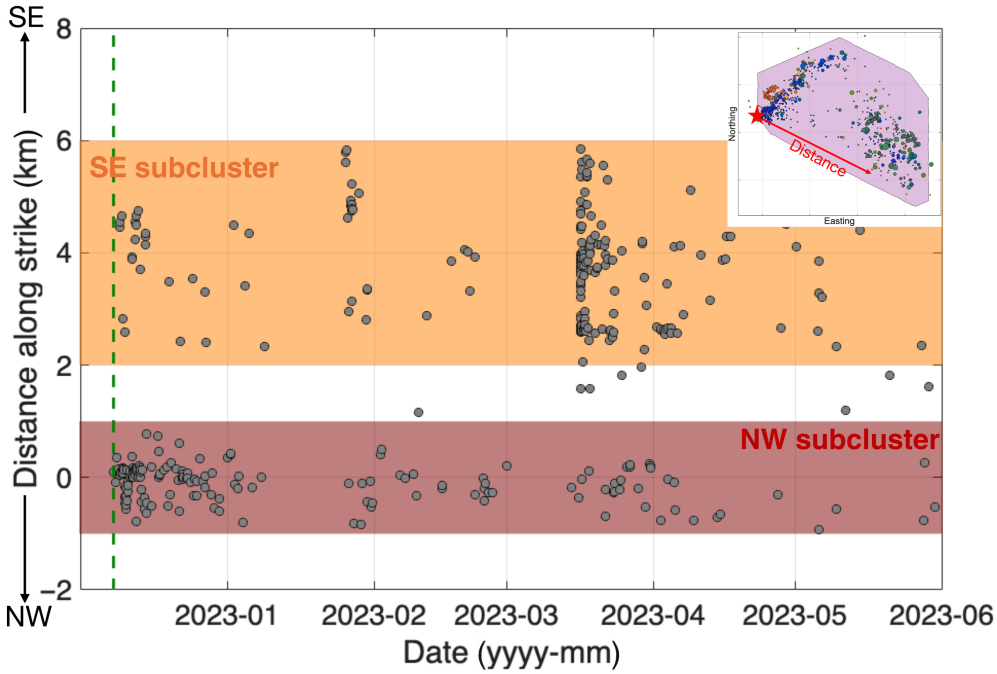

Figure 6. Evolution of seismicity along the mainshock fault plane (MFP) with time. The distance plotted on the *y-axis* represents the horizontal distance of each event along the strike of the fault (120°) from the up-dip, northwestern vertex of the MFP. The inset map, adapted from Figure 4a, shows the geometry of this plot construction: the red star shows the up-dip northwest vertex with distances computed along an azimuth of 120° from this point. The red and orange patches in the main figure show the approximate positions of the northwest and southeast subclusters, and the green dashed line shows the start of monitoring with the local arrays. At early times, seismicity was focused at a distance of 0 km, that is, at the northwest end of the MFP. The color version of this figure is available only in the electronic edition.

We note a quiescent zone in the middle of the MFP, which separates the seismicity into a denser northwestern subcluster and a more diffuse southeastern subcluster. This quiescent zone may represent the area in which the M_L 5.6 mainshock nucleated—in this area, the stresses will have been released entirely by the mainshock, leaving few aftershocks. If so, the events in the northwest and southeast subclusters would represent aftershocks occurring on either side of the mainshock rupture, where stresses have concentrated after the mainshock. This type of aftershock behavior—forming a halo around a quiescent zone where stresses were fully released by the mainshock—is commonly observed for tectonic faulting (e.g., Mendoza and Hartzell, 1988) and has been observed in previous cases of induced seismicity as well (Kettlety *et al.*, 2021).

In Figure 6, we show the evolution of seismicity along the MFP with time. We do this by computing the horizontal position of each event along the strike of the MFP, with distance being computed from the position of the up-dip, northwestern vertex of the MFP (see Fig. 6 inset). In this figure, we only show events above the magnitude of completeness for both clusters ($M_L \geq 0.6$) to avoid introducing any spatial bias in detection performance. The PRISM array was installed 6 days after the mainshock, so detailed observations of events in the immediate aftermath of this event are not available. However, the seismicity that has been recorded shows a clear pattern of temporal

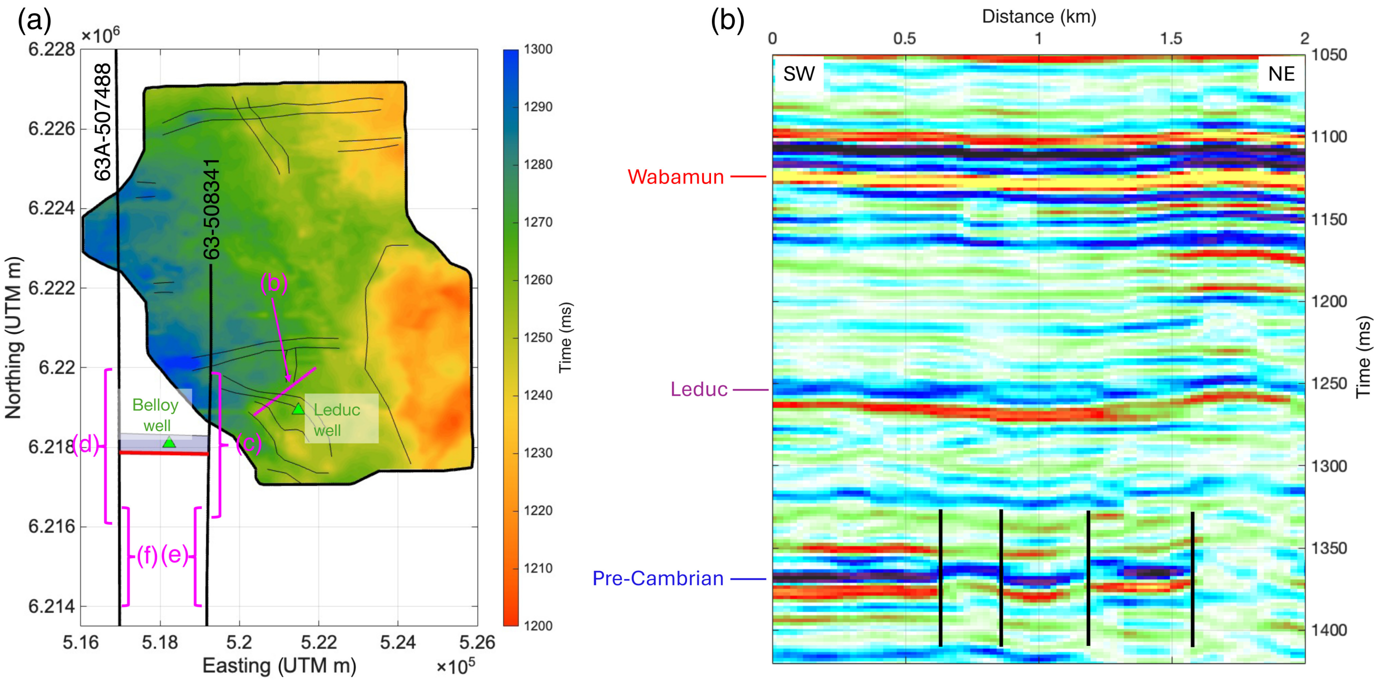

Figure 7. Reflection seismic sections in the vicinity of the Reno seismicity. Panel (a) provides a map showing the 2D and 3D seismic coverage. The thick black lines show the positions of the 2D seismic lines. The colors show the structure of the basement horizon within the 3D seismic cube. The thin black lines show basement horizon faults mapped in the 3D seismic section, and the thick red line shows the Belloy fault mapped from the 2D seismic. Magenta lines and brackets show the positions of the seismic sections plotted in panels (b–f). In panel (b), we show a section through the 3D seismic cube showing faults offsetting the basement. These faults could potentially extend to the Leduc Formation, but do not extend above the Leduc. In panels (c) and (d), we show 2D sections from lines 63-508341 and 63A-507488 where a basement-rooted normal fault (annotated by the thick-black line) is observed cutting strata through to the Belloy Level (above the Upper DTM horizon). In panels (e) and (f), we show 2D sections from lines 63-508341 and 63A-507488 at the position where the MFP, if extrapolated up-dip from its position as mapped by the seismic events (see Fig. 4), would subcrop at the basement (Pre-Cambrian) horizon. No offset is observed at the basement horizon at this position. The color version of this figure is available only in the electronic edition. (*Continued*)

evolution. Although there are events occurring across the entire fault plane throughout the monitoring period, the focus of the seismicity evolves from the northwest to the southeast of the MFP with time. From December 2022 to January 2023 (a period representing the early phase of aftershocks after the M_L 5.6 event), the bulk of the seismicity is focused at the northwest edge of the MFP: in the first month of deployment, the northwest subcluster contained 112 events (above M_c), whereas the southeast subcluster contained only 26 events. In contrast, from March 2023 onward, the northwest cluster contained 74 events, whereas the southeast cluster contained 165 events. The location of the second-largest event, the M_L 5.1 event on 16 March 2023, which is located in the southeast cluster, is consistent with this pattern of seismicity moving from northwest to southeast during the monitoring period.

Pre-Existing Faults Imaged by Reflection Seismic Surveys

The Reno seismicity is located within the crystalline basement, with the shallowest events being 3700 m below the surface. The Leduc Well has a maximum vertical depth of 1923 m, meaning a vertical separation of over 1.7 km between the well and the shallowest events. The Belloy Well has a maximum vertical depth of 792 m below surface, giving a vertical separation of approximately 3 km to the events.

However, this vertical separation does not preclude an induced cause for the events because stress or pressure perturbations caused by industrial activities in the sedimentary section can be passed downward into underlying basement rocks (e.g., Verdon, 2014; Galloway *et al.*, 2018; Wang *et al.*, 2020; Verdecchia *et al.*, 2021). The most common processes invoked for this is the existence of pre-existing faults providing either a hydraulic connection for pore pressure transfer, or a geomechanical connection for stress transfer (e.g., Eyre *et al.*, 2019; Peña-Castro *et al.*, 2020), into the basement. Therefore, an understanding of the pre-existing faulting in the area is necessary to fully understand induced seismicity causation. The area of interest for the Reno sequence is partially covered by a 3D seismic survey, with additional 2D lines providing further coverage. We use the reflection seismic data to map existing faults, with a

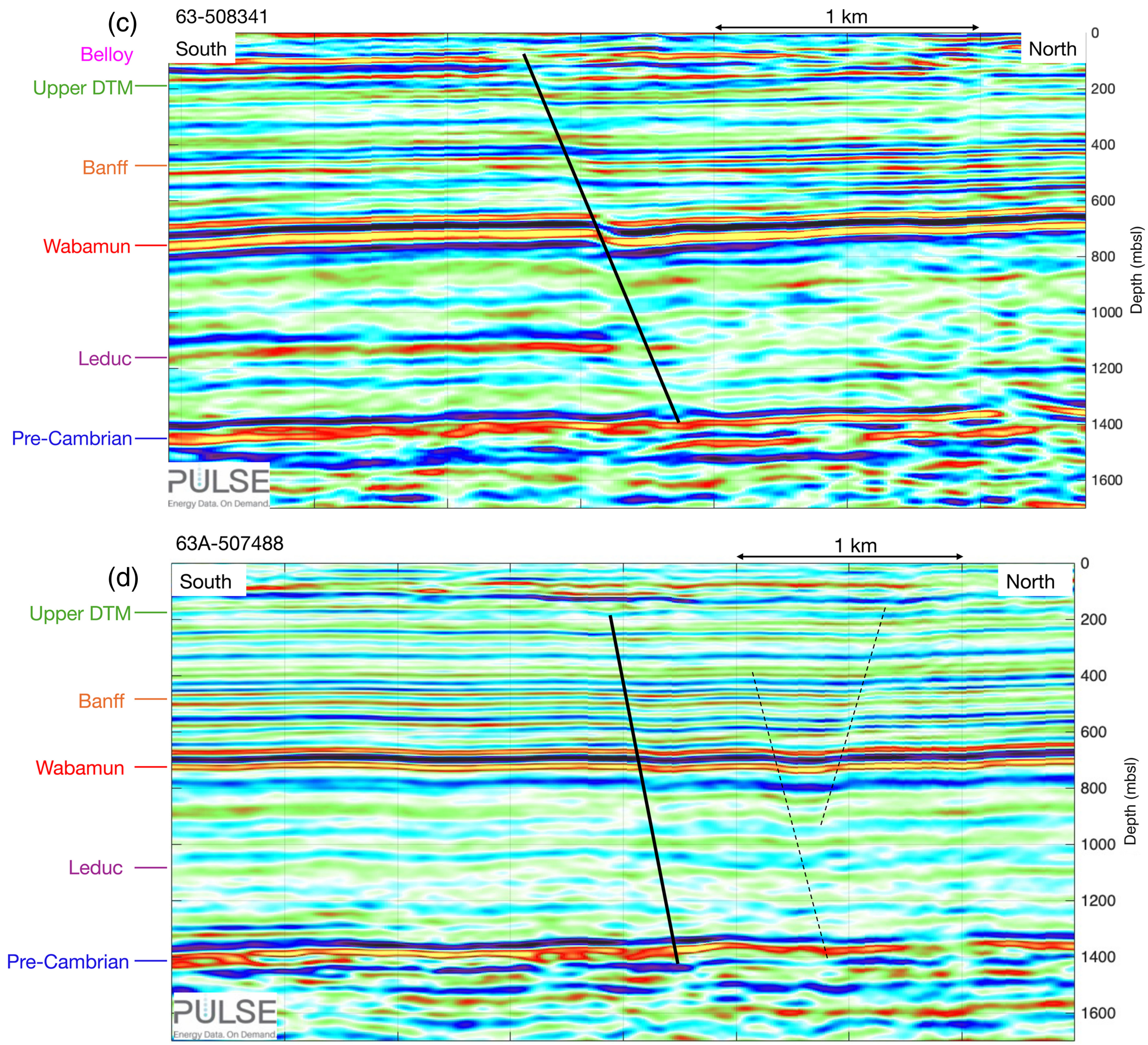

Figure 7. Continued

particular focus on faults that cut sedimentary strata and run downward into the basement and therefore could serve as conduits for downward transfer of pressure or stress to the location of the mainshock. Fault mapping was done using a combination of manual analysis and the use of coherence and similarity attributes.

Figure 7a provides a map of the 3D seismic reflection cube and 2D lines that are available in the area from seismic vendors. Figure 7b–d shows examples of mapped faults within vertical seismic sections. A fault is observed near the Belloy Well on the two 2D seismic lines (Fig. 7c,d). This structure is observed to cut the entire Palaeozoic section, from the basement through to the Belloy Formation. We refer to this fault as the Belloy fault hereafter. Several faults are also observed near the Leduc Well (Fig. 7b). These are observed to offset the basement, potentially extending into the overlying Leduc Formation, but no further upward. We refer to these faults, which are observed only at the interface between the basement and the sediments, as "basement horizon faults" hereafter. Figure 7a maps the positions of the identified faults. Figure 8 shows the positions of the identified faults relative to the WWD wells and the Reno seismicity. Neither the Belloy fault nor the basement horizon faults can

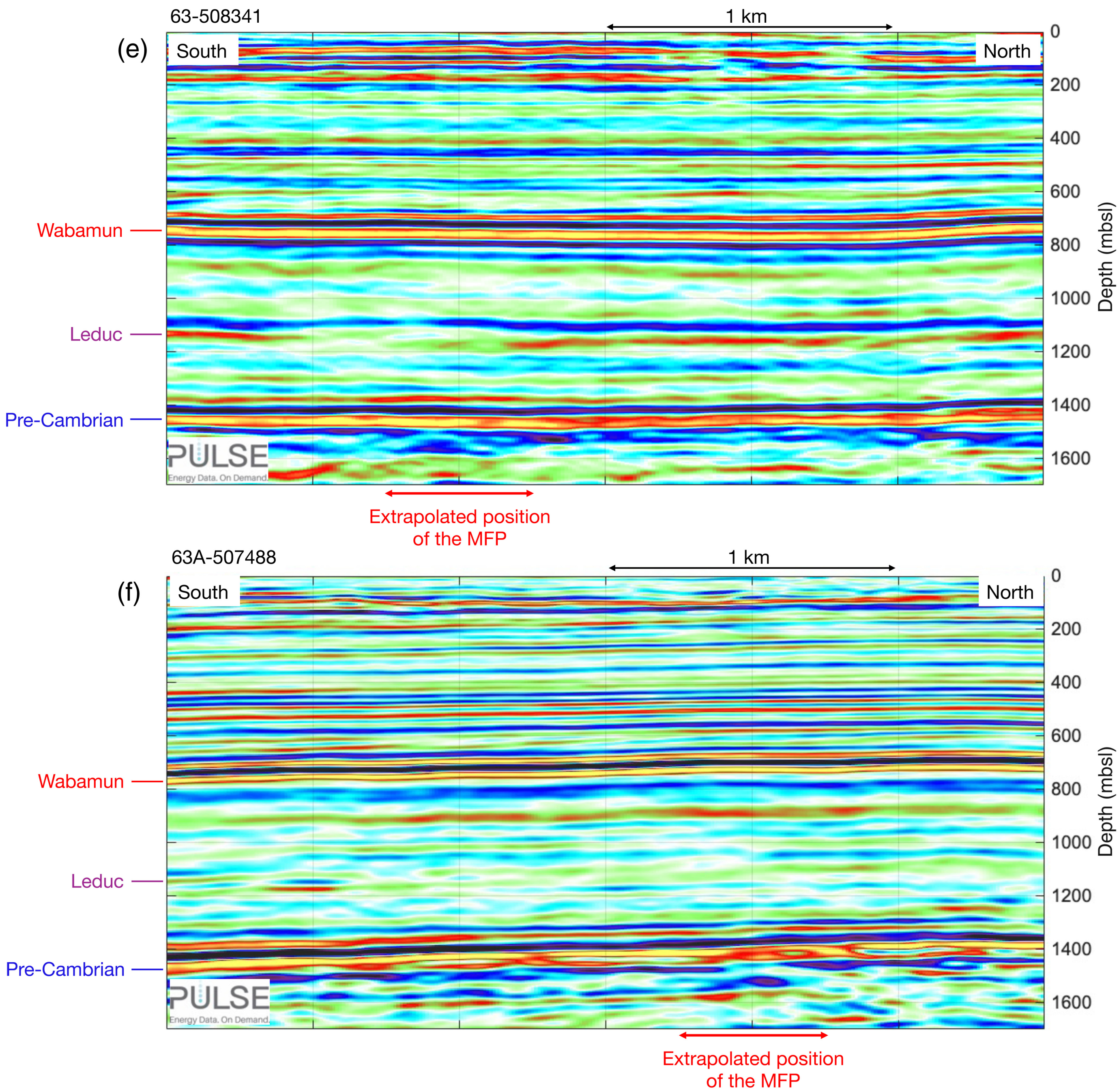

Figure 7. Continued

be tracked within the basement. This is because of the lack of horizontal reflectors in the crystalline basement rocks. The Belloy fault is mapped across a depth range of more than 1 km, offsetting layers spanning over 200 million years of geological time. Therefore, it is reasonable to assume that this fault may extend some distance into the basement.

We note that the Belloy fault is interpreted based on the observation of this feature at two 2D seismic lines (Fig. 7c, d). It has a west–east strike, which is consistent with other local faults seen at the basement horizon (see Fig. 6c), and is also consistent with a subset of the focal mechanisms observed by Gu *et al.* (2025), who found some events with a west–east strike and a reverse fault mechanism. However, care should be taken when interpreting faults observed on 2D seismic lines because no interpretation can be fully constrained. Our interpretation of a single fault running west–east between the 2D lines is the most parsimonious. However, other interpretations, such as two en echelon faults with strikes that are oblique to the

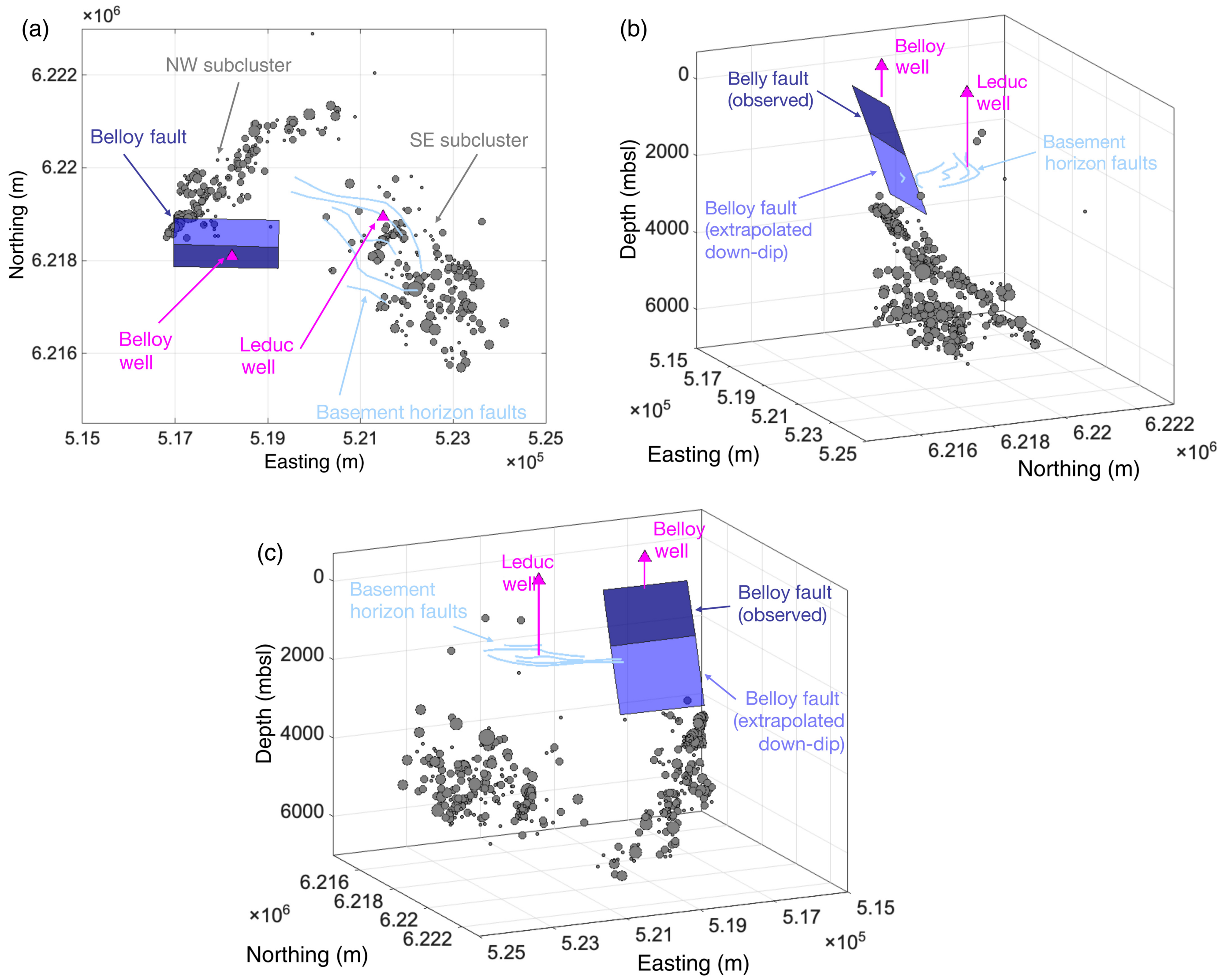

Figure 8. (a) Map and (b,c) 3D views showing the position of the faults mapped in the reflection seismic data (Fig. 7) relative to the Reno seismicity (gray dots). The dark-blue plane shows the position of the Belloy fault as observed in the reflection seismic sections, whereas the light-blue plane shows an extension of this plane downward along the same strike and dip. The basement horizon faults near the Leduc Well are plotted with light blue lines at the depth of the basement. The extended Belloy fault plane intersects the shallowest, densest cluster of seismicity at the western end of the MFP. The color version of this figure is available only in the electronic edition.

2D seismic lines, could be made. Whichever interpretation is preferred, the observations clearly show that there are faults that penetrate from the basement into the Belloy Formation in the immediate vicinity of the Belloy Well. Basement-rooted faults extending upward into the Belloy Formation have been documented throughout the Peace River Arch, including in this area (Henderson *et al.*, 1994; Eaton *et al.*, 1999; Hope *et al.*, 1999; Weides *et al.*, 2014).

Based on the aforementioned analysis, we identify three potential routes by which perturbations—either pore pressure increases or geomechanical processes (e.g., Eyre *et al.*, 2019; Peña-Castro *et al.*, 2020)—could have been transferred from the WWD targets in the sedimentary section downward into the basement. These are: (1) an upward continuation of the MFP into the sedimentary section, (2) the Belloy fault, or (3) the basement-horizon faults near the Leduc Well. We consider each of these possibilities in turn.

Our event locations place the seismicity more than 1 km below the basement interface. The absence of seismic events at shallower depths indicates that the MFP does not continue upward into the sedimentary section. This interpretation can be further examined using the reflection seismic observations. Extrapolating the MFP up-dip (assuming a constant strike and dip), we can estimate the positions where the MFP would subcrop against the basement-sediment interface on the 2D seismic lines shown in Figure 7. Reflection seismic sections at these positions are shown in Figure 7e,f: the approximate positions where the MFP would subcrop at the basement-sediment interface are marked. We find that the Precambrian horizon at these positions is flat, with no evidence for faulting observed. The MFP is a large structure (capable of hosting multiple M > 5.0 events), and it appears to be a reverse fault, so vertical offsets across the fault should be expected. Given the size of this fault, the expected offset should be well within the resolution of the reflection seismic data (e.g., Nantanoi *et al.*, 2022). Hence, the absence of any observed disturbance in the basement horizon at the expected subcrop of the MFP provides evidence that this feature does not reach the sedimentary section.

The Belloy fault is mapped across a significant depth range through the sedimentary section. It lies within 250 m of the Belloy Well. If the mapped fault plane is assumed to extend with a constant strike and dip into the basement, then it intersects the uppermost part of the seismic event cluster at the western end of the MFP (at a vertical position 1.7 km below the basement-sediment interface, see Fig. 8).

This interpretation is robust to this uncertainty in fault interpretation on the 2D seismic lines: the 63-508341 seismic line runs within 1 km of the Belloy Well. The fault mapped at this line shows offsets across a large thickness of the lower Palaeozoic. Therefore, it is implausible that it would not extend a reasonable distance (i.e., 100s of m) on either side of the line. Even if the faults were mapped with a different strike (i.e., the en echelon interpretation as advanced earlier), they would still run within proximity of the Belloy Well. The northward dips as observed in the reflection seismic would, if extrapolated into the basement, place the "toe" of any structure near to the top of the MFP at its northwest end, regardless of what is assumed with respect to the fault strike.

The intersection of the Belloy fault at the up-dip, northwest end of the MFP represents the shortest possible vertical distance through the basement, as this is where the seismicity on the MFP is shallowest. Figure 6 documents an evolution in the observed seismicity moving from the northwest to the southeast along the MFP. It is notable that the point of intersection between the MFP and the extrapolated continuation of the Belloy fault occurs where seismicity was densest during the earliest phase of the monitoring period (representing the earliest phases of aftershocks following the M_L 5.6 mainshock). It should be recognized that the spatial evolution of the observed seismicity could be driven by a range of complex geomechanical effects. However, the most parsimonious interpretation of the observed spatial evolution in the seismicity from northwest to southeast is that it indicates the perturbations (whether pressure or other geomechanical effects) that triggered the seismicity first impacted the MFP at its northwest end. Hence, the observed spatial evolution is consistent with the Belloy fault providing a route for pressure or stress perturbations to propagate downward to the MFP at its northwest end, with the seismicity then moving laterally along the MFP from northwest to southeast.

The basement horizon faults near to the Leduc Well (shown in Fig. 7b) also represent a possible mechanism for downward transfer of pressure and/or stress perturbations from the Leduc Formation, which sits just above the basement (see Fig. 1). The dips of the basement horizon faults are less well constrained given their relatively short vertical extent (they can only be reliably observed offsetting the basement reflector), but if they were extrapolated vertically downward, these faults would intersect the southeastern, down-dip end of the MFP. Because it dips to the northeast, the MFP is significantly deeper below the Leduc Well, and the vertical separation between the basement-sediment interface and the MFP, at approximately 3.7 km, is significantly larger at this position when compared to the 1.7 km vertical separation from the basement-sediment interface to the up-dip edge of the mainshock plane where the Belloy fault is situated.

The observed spatiotemporal evolution of the seismicity (Fig. 6) with respect to these faults represents the opposite situation to that of the Belloy fault: at the onset of the monitoring, seismicity was much lower at the southeast end of the MFP. Most of the seismicity at the southeast end emerged later in the sequence, and the density of the seismicity at the southeast end of the MFP is lower than at the northwest end.

In summary, the reflection seismic data suggest that the MFP does not subcrop at the basement-sediment interface. Instead, the reflection seismic observations reveal two plausible pathways that could have provided a hydraulic or geomechanical connection from WWD activities in the sedimentary section to the MFP in the basement: the Belloy fault, and the basement-horizon faults near to the Leduc Well. The extrapolated down-dip extension of the Belloy fault connects to the shallowest part of the MFP, in the area where the seismicity was observed in the immediate aftermath of the M_L 5.6 event, and where the seismicity was densest. In contrast, the basement horizon faults near to the Leduc Well, if extended vertically through the basement, would connect to a deeper section of the MFP, to a part of the MFP where the seismicity was much lower during the early stages of the sequence, and was less dense. These seismological and geophysical observations indicate that the mapped Belloy fault was the most likely conduit of pressure and/or stress transfer from WWD activities in the sediments to the MFP in the basement.

Discussion

Implications for induced seismicity attribution

The Belloy fault cuts through both the Leduc and Belloy Formations (see Fig. 7). Hence, pressure or geomechanical perturbations in either the Belloy and/or Leduc Formations could have been transferred downward by this structure. Triggering of seismicity by WWD activities in both the Belloy and Leduc Formations has been observed elsewhere in the WCSB (Horner *et al.*, 1994; Schultz and Wang, 2020).

Geomechanical models could be developed to better understand the perturbations caused by WWD activities in the

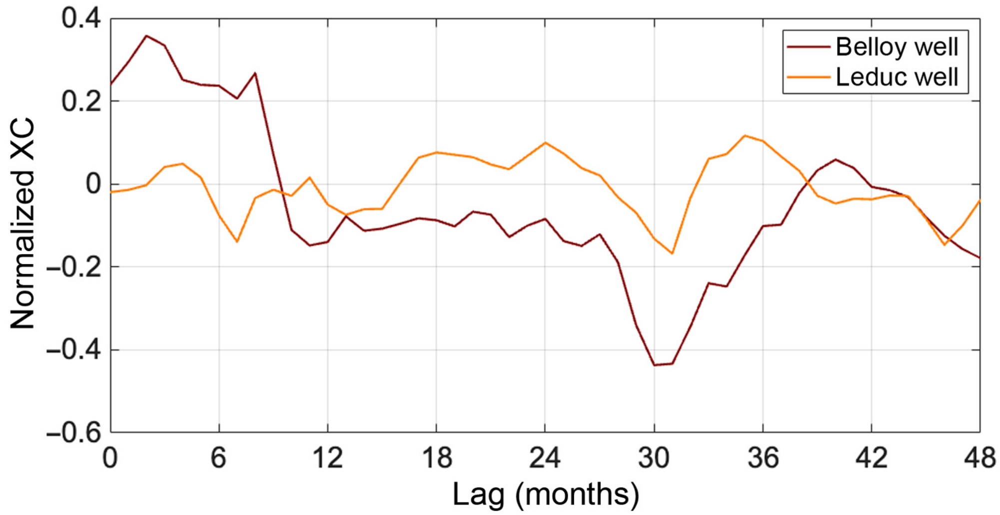

Figure 9. Normalized cross-correlation coefficients as a function of time lag between the rate of seismicity in the Reno sequence and injection rates in the Leduc Well (orange) and Belloy Well (red). A peak in cross-correlation is observed at short-time lags for the Belloy Well. The color version of this figure is available only in the electronic edition.

Belloy and Leduc Formations to further resolve the respective contributions from the Belloy and Leduc Wells discussed in this study. However, to be of use such models would need to be constrained by pressure and geomechanical observations, which are of limited availability during the period of interest, hence our reliance on the observed spatial and temporal relationships between the injection activities and the seismicity in this study. We note that the need for regular collection of relevant pressure and geomechanical observations at future sites to enable such modeling should be recognized.

The Belloy Well (within 250 m laterally) is significantly closer to the Belloy fault than the Leduc Well (>2 km to the northeast). The Belloy Well (3.6×10^5 m^3 as of 12 January 2023) has injected a lower cumulative volume than the Leduc Well (1.3×10^6 m^3), although injection rates were similar in both wells at the time of the 2022 mainshock (see Fig. 2). Consideration must also be given to potential contributions to pressure change in the Leduc Formation from high-volume WWD wells located over 15 km to the north of the Reno sequence. Although they are more distant, they have injected significantly higher volumes and so could have contributed to pore pressure changes in the Leduc Formation at the location of the Reno sequence. Both formations have good hydraulic properties in general (Samaroo *et al.*, 2023), although the Leduc is significantly thicker, especially since the Belloy Formation is eroded by the Pre-Cretaceous unconformity in this area (see Fig. 1). The Belloy Formation is shallower; however, there is pervasive evidence in the WCSB for pressure and stress perturbations caused by industrial activities within upper Palaeozoic and Triassic strata being transferred over significant vertical thickness (of several kilometers) to reactivate faults in the underlying basement (e.g., Schultz *et al.*, 2014; Hosseini and Eaton, 2018; Peña-Castro *et al.*, 2020; Wang *et al.*, 2021, 2022, 2023; Roth *et al.*, 2022). We note that other wells in this area have reported lost circulation incidents when drilling through the Belloy Formation (based on proprietary industry data), providing circumstantial evidence that faults cutting the Belloy Formation are receptive to the ingress of fluids.

Further insight into potential induced seismicity causation can be obtained by examining the temporal correlation between WWD rates and the rates of induced seismicity (e.g., Oprsal and Eisner, 2014; Schultz and Telesca, 2018). In performing this assessment, we use the earthquake catalog sourced from regional seismic networks (AGS, 2020, shown in Fig. 2) to avoid any bias caused by the improvements in local detection thresholds with the deployment of the local arrays from late 2022 onward. The available injection rate data (Fig. 2b) are binned at 1-month intervals, and we bin the earthquake data likewise, computing the rate of seismicity above a magnitude of completeness of $M_c = 1.5$. The analysis for each well spans from the onset of injection (December 2012 for the Leduc Well, September 2016 for the Belloy Well) until January 2024. In the following analysis, we did not decluster the seismicity catalog: an equivalent analysis using a declustered catalog is presented in Figure SF7. Following Schultz and Telesca (2018), we subtracted the mean from each time series to avoid spurious correlations between series with large means and low standard deviations. We calculated cross-correlation coefficients as a function of time-lag between the normalized injection and seismicity time series, up to a maximum time-lag of 4 yr. Figure 9 shows the results.

For the Leduc Well, the correlation coefficients are low, regardless of time lag. There is no temporal correlation observed between injection activities in the Leduc Well and the Reno seismicity. In contrast, for the Belloy Well, we observe high correlation coefficients at short time-lags (less than 10 months). The correlation coefficient peaks at a value of 0.36 for a time lag of 2 months.

We assessed the statistical significance of this outcome using a selection of methods. First, we used the Student's t-test, evaluated at

$$t = \frac{R\sqrt{N-2}}{\sqrt{1-R^2}},$$

in which R is the observed correlation coefficient, and N is the number of samples in the cross-correlation. In effect, this test describes the likelihood of obtaining the observed value of R if the null hypothesis (i.e., the injection and seismicity time series were independent and uncorrelated) were true. This test produced a statistical significance for the observed correlation of $p > 99\%$.

Next, We used the reshuffling test described by Schultz and Telesca (2018), where the injection time series are randomly reshuffled while preserving spectral amplitudes to preserve any cyclic autocorrelation. Cross-correlation coefficients are then computed for these surrogate randomized time series, and the observed coefficient is compared against the distribution of surrogate values to determine the likelihood of obtaining this value from randomized data with the same spectral properties. We performed 2000 test iterations using this method. This test produced a statistical significance for the observed correlation of $p = 96\%$. We also used an alternative reshuffling test, based on Grigoratos *et al.* (2020), where the injection time series is offset randomly in time. This offset is cyclical, such that an offset beyond the final date of the analysis window is reset back to the start of the window. As aforementioned, correlation coefficients are computed for the surrogate randomized time series to determine the likelihood of obtaining the observed correlation by chance. Again, we performed 2000 test iterations using this method. This test produced a statistical significance for the observed correlation of $p = 97\%$. Similar values were produced using a declustered earthquake catalog (Fig. SF7).

In contrast, the statistical significance of the maximum observed correlation coefficient between the seismicity rates and the injection in the Leduc Well (a maximum cross-correlation coefficient of 0.12) were $p = 0.8\%$ (using the Student's *t*-test), $p = 16\%$ (using the Schultz and Telesca, 2018 method), and $p = 42\%$ (using the temporal reshuffling test), therefore by all methods there is a greater than 50% chance of the observed correlation with the Leduc Well being obtained by chance.

Therefore, we conclude that there is a temporal correlation between WWD in the Belloy Well and the Reno seismicity. Qualitatively, this temporal correlation with the Belloy Well is driven by the fact that the seismicity initiated in 2017, a few months after injection began (September 2016), and that the injection rate more than doubled in April 2022, a few months before the seismicity accelerated in November 2022 (see Fig. 2b).

In this area, the Belloy Formation subcrops against the Pre-Cretaceous unconformity, which limits the thickness of the Belloy Formation available for WWD. The limited formation thickness would facilitate increased pressure within this formation: with the Belloy Formation thinning against the overlying unconformity, the injected water may have had nowhere else to go. The close proximity of the Belloy fault (within 250 m of the Belloy Well) would therefore have provided a conduit for downward transfer of pressure or stress to the MFP, providing a reasonable mechanism to account for the observed correlation between injection in the Belloy Well and the Reno seismicity.

We recognize that induced seismicity attribution can be challenging, and it is not always possible to reach definitive conclusions. Pressure perturbations from WWD operations in both the Leduc and Belloy Formations could have been transferred downward to the MFP by the Belloy fault. Nevertheless, the available evidence points toward the Belloy Well as having the strongest connection with the Reno seismicity because it is in very close proximity to the Belloy fault, and WWD operations in this well have a statistically significant temporal correlation with the Reno seismicity. It is also possible that increased pressures in the Leduc Formation could have preconditioned the fault for failure, with the contribution from the Belloy Well serving as the ultimate trigger for the seismicity. This being the case, further work may be necessary to determine the relative contributions to the overall pressure increases in the Leduc Formation from the nearby well versus the higher volume but more distant wells to the north.

Comparing our results with previous studies of the Reno sequence

The Reno seismicity sequence has been previously studied by Schultz *et al.* (2023), Vasyura-Bathke *et al.* (2023), Li *et al.* (2024), and Gu *et al.* (2025). Schultz *et al.* (2023) and Vasyura-Bathke *et al.* (2023) used regional seismic observations, which had significantly lower resolution than the local arrays used in this study. Both studies also used InSAR data to constrain the mainshock rupture. The location of our MFP within the basement is consistent with these studies. Similarly, the orientation of our MFP is consistent with the mainshock ruptures estimated in these studies. Our fault plane has a strike of 300° and a dip of 43°. Schultz *et al.* (2023) have a strike of 297° and a dip of 58°, whereas Vasyura-Bathke *et al.* (2023) have a strike of 310° and a dip of 45°.

Vasyura-Bathke *et al.* (2023) further separated their earthquake population into multiple, distinct, subparallel, en echelon fault planes. However, we find no evidence from our aftershock hypocenters to support this interpretation: our locations are well fitted by a single fault plane with an orientation that matches the mainshock focal mechanism. The dimensions of our single plane, roughly 30 km^2, are within the range of expected rupture dimensions for an M_L 5.6 event.

Li *et al.* (2024) used the PRISM array round 1 data from December 2022 to January 2023. They processed the data with automated machine learning tools of the type that are becoming increasingly common in seismological analyses (Zhu and Beroza, 2019; Mousavi *et al.*, 2020). Li *et al.*'s hypocenter distribution showed significantly higher spatial scattering, with events located throughout the sedimentary column to very shallow depths. Location uncertainties reported by Li *et al.* (2024) were high (average errors close to 1 km for their best-performing model). Depth pooling at velocity model boundaries in Li *et al.*'s analysis produced horizontal, linear event clusters in the subsurface that are artefacts and do not represent actual subsurface structures. Given the high scatter in their dataset, Li *et al.* (2024) were not able to identify any discrete fault planes from their hypocenter locations.

The use of machine learning for seismological processing tasks has shown significant promise in recent years (e.g., Kong *et al.*, 2019). Machine learning tools have been used to improve the characterization of induced seismicity cases elsewhere (e.g., Park *et al.*, 2022). However, the high scatter and uncertainties in the Li *et al.* (2024) dataset mean that their results do not help understand the mechanisms that have caused the Reno sequence. This serves as a cautionary note with respect to the use of machine learning tools in situations where seismological results are used to inform regulatory decisions that could have significant financial and/or reputational implications. In such situations, careful manual processing of seismic data may be required, rather than reliance on machine learning tools in the absence of rigorous quality control steps.

Gu *et al.* (2025) also estimated event locations using the PRISM array data. The focus of their article was on describing the performance of the nodal monitoring array, and so they did not investigate in any detail the subsurface structures mapped out by the event locations, or their relationships to the different disposal wells. A visual comparison between our locations and figure 4 of Gu *et al.* (2025) suggests that our event epicenters are similar. Gu *et al.* (2025) did not report event depths, so it is not possible to assess whether their depths match our locations, but we note that Gu *et al.* used a regional velocity model and did not attempt to calibrate V_P/V_S ratios based on picking residuals. Gu *et al.* (2025) suggested a potential relationship between disposal volumes in the Leduc Well and the seismicity rates, but did not provide any quantitative analysis to support this assertion.

Conclusions

The M_L 5.6 Reno mainshock represents the largest induced earthquake to have occurred in Canada, and one of the largest induced events anywhere in the world. In this study, we have analyzed the aftershocks from this event recorded by local seismic arrays. The event locations map out a single plane at depths of 3.7–7 km below the surface, within the crystalline basement. The orientation and position of this plane are consistent with regional seismic and InSAR observations of the mainshock rupture. We conclude that the plane mapped out by the event hypocenters represents the fault plane that ruptured in the M_L 5.6 mainshock.

We used reflection seismic data to map pre-existing structures that could have provided a mechanism to transfer stress and/or pressure perturbations from injection depths into the basement. We identified the Belloy fault running through the entire Palaeozoic sedimentary section, from the basement to the Belloy Formation, which, if extrapolated down-dip through the basement, would intersect the MFP at its shallowest point, where the seismicity was densest during the early stages of the monitoring, and where the density of seismic activity was highest overall. We also identified other faults offsetting the basement horizon. However, these faults, if extrapolated through the basement, would intersect the MFP at greater depths, in a region where the seismicity was lower during the early stages of monitoring, and where events are more diffuse overall. Therefore, we conclude that the Belloy fault represents the most likely conduit for downward pressure transfer from the sedimentary section to the MFP in the crystalline basement.

The Belloy fault runs through both the Belloy and Leduc Formations, and so pressure perturbations in either formation could have been transferred downward by this structure. The Belloy Well is significantly closer to the Belloy fault, and we find statistically significant temporal correlation between the seismicity and WWD into the Belloy Well, whereas no temporal correlation is observed for WWD into the Leduc Well. These observations lead us to conclude that, of the two nearby WWD wells, the Belloy Well has a stronger connection to the Reno induced seismicity sequence.

Data and Resources

The seismic monitoring data recorded by the Peace River Induced Seismic Monitoring (PRISM) array were provided to them by the Alberta Geological Survey (AGS). The continuous waveform data will be available from the Incorporated Research Institutions for Seismology (IRIS) with Network Code 3W (see Gu *et al.*, 2025 for details). The seismic monitoring data recorded by the operator array were available from IRIS with network code I0, stations LOY01–LOY05. The reflection seismic data shown in Figure 7 are proprietary and we do not have permission to share. The regional earthquake catalog shown in Figure 2 is available from the Alberta Earthquake Dashboard (AGS, 2020; https://ags-aer.shinyapps.io/Seismicity_waveform_app/). Wastewater disposal (WWD) well information is available from Petrinex, Canada's Petroleum Information Network (https://www.petrinex.ca/PD/Pages/APD.aspx). Both the websites were last accessed in September 2025. The earthquake catalog generated in this study is provided as supplemental material.

Declaration of Competing Interests

The authorship team was appointed by Obsidian Energy Ltd., who are the operator of the 100/14-18-082-17W5/00 well (the Leduc Well), to assess the causative mechanisms of the Reno earthquake sequence. We were tasked to provide Obsidian with a detailed subsurface analysis to understand the relationships between the seismicity, geological structures, and nearby disposal wells. The authorship team worked independently from Obsidian, and Obsidian had no input into the conclusions reached in this article.

Acknowledgments

The authors would like to thank Obsidian Energy Ltd. for providing the 3D seismic reflection cube shown in Figure 7. The authors would like to thank Pulse Seismic Inc. for providing the 2D seismic reflection lines shown in Figure 7. The authors would like to thank the Alberta Geological Survey (AGS) for providing the seismic monitoring data from the Peace River Induced Seismic Monitoring (PRISM) array. J. P. V. received additional funding to support this study from the UK Natural Environment Research Council (NERC) SeisGreen Grant (Grant Number NE/W009293/1). The authors would like to thank the Associate Editor for their effort with their article, and Hongyu Yu, Ryan Schultz, and two anonymous reviewers for their constructive reviews.

References

Alberta Energy Regulator (AER) (2023). Environmental Protection Order made by the Alberta Energy Regulator on 23rd March, 2023, available at https://www1.aer.ca/compliancedashboard/enforcement/202303-46_Obsidian%20Energy%20Ltd_Order.pdf (last accessed March 2025).

Alberta Geological Survey (AGS) (2020). Alberta Earthquake Dashboard, *Alberta Geol. Surv.*, available at https://ags.aer.ca/publications/all-publications/iam-005 (last accessed March 2025).

Angus, D. A., Q. J. Fisher, J. M. Segura, J. P. Verdon, J.-M. Kendall, M. Dutko, and A. J. L. Crook (2016). Reservoir stress path and induced seismic anisotropy: Results from linking coupled fluid-flow/geomechanical simulation with seismic modelling, *Pet. Sci.* **13,** 669–684.

Bell, J. S., P. R. Price, and P. J. McLellan (1994). In-situ stress in the Western Canada Sedimentary Basin, in *Geological Atlas of the Western Canada Sedimentary Basin*, G. D. Mossop and I. Shetsen (Editors), Canadian Society of Petroleum Geologists and Alberta Research Council, Calgary, Canada.

Block, L. V., C. K. Wood, W. L. Yeck, and V. M. King (2014). The 2024 January 2013 M_L 4.4 earthquake near Paradox, Colorado, and its relation to deep well injection, *Seismol. Res. Lett.* **85,** 609–624.

Eaton, D. W., G. M. Ross, and J. Hope (1999). The rise and fall of a cratonic arch: A regional seismic perspective on the Peace River Arch, Alberta, *Bull. Can. Petrol. Geol.* **47,** 346–361.

Eyre, T. S., D. W. Eaton, D. I. Garagash, M. Zecevic, M. Venieri, R. Weir, and D. C. Lawton (2019). The role of aseismic slip in hydraulic fracturing–induced seismicity, *Sci. Adv.* **5,** eaav7172, doi: 10.1126/sciadv.aav7172.

Foulger, G. R., M. W. Wilkinson, M. P. Wilson, N. Mhana, T. Tezel, and J. G. Gluyas (2023). Human-induced earthquakes: E-PIE—A generic tool for evaluating proposals of induced earthquakes, *J. Seismol.* **27,** 21–44.

Galloway, E., T. Hauck, H. Corlett, D. Pană, and R. Schultz (2018). Faults and associated karst collapse suggests conduits for fluid flow that influence hydraulic fracturing-induced seismicity, *Proc. Natl. Acad. Sci.* **115,** E10003–E10012.

Goebel, T. H. W., M. Weingarten, X. Chen, J. Haffener, and E. E. Brodsky (2017). The 2016 Mw 5.1 Fairview, Oklahoma earthquakes: evidence for long-range poroelastic triggering at > 40 km from fluid disposal wells, *Earth Planet. Sci. Lett.* **472,** 50–61.

Grigoratos, I., E. Rathje, P. Bazzurro, and A. Savvaidis (2020). Earthquakes induced by wastewater injection, Part II: Statistical evaluation of causal factors and seismicity rate forecasting, *Bull. Seismol. Soc. Am.* **110,** 2483–2497.

Gu, Y. J., W. Sun, T.-C. Yu, J. Wang, R. Wang, T. Li, and R. Schultz (2025). Peace River Induced Seismic Monitoring (PRISM) nodal seismic array, *Seismol. Res. Lett.* **96,** 562–575.

Henderson, C. M., B. C. Richards, and J. E. Barclay (1994). *Permian strata of the Western Canada Sedimentary Basin: In Geological Atlas of the Western Canada Sedimentary Basin*, G. D. Mossop and I. Shetsen (Editors), Canadian Society of Petroleum Geologists and Alberta Research Council, Calgary, Canada.

Hope, J., D. W. Eaton, and G. M. Ross (1999). Lithoprobe seismic transect of the Alberta Basin: Compilation and overview, *Bull. Can. Petrol. Geol.* **47,** 331–345.

Horner, R. B., J. E. Barclay, and J. M. MacRae (1994). Earthquakes and hydrocarbon production in the Fort St. John area of northeastern British Columbia, *Can. J. Explor. Geophys.* **30,** 39–50.

Hosseini, B. K., and D. W. Eaton (2018). Fluid flow and thermal modeling for tracking induced seismicity near the Graham disposal well, British Columbia (Canada), *SEG 88th Annual Conference*, Anaheim, California, Expanded Abstracts, 4987–4991.

Igonin, N., J. P. Verdon, and D. W. Eaton (2022). Seismic anisotropy reveals stress changes around a fault as it is activated by hydraulic fracturing, *Seismol. Res. Lett.* **93,** 1737–1752.

Igonin, N., J. P. Verdon, J.-M. Kendall, and D. W. Eaton (2021). Large-scale fracture systems are permeable pathways for fault activation during hydraulic fracturing, *J. Geophys. Res.* **126,** e2020JB020311, doi: 10.1029/2020JB020311.

Kettlety, T., J. P. Verdon, A. Butcher, M. Hampson, and L. Craddock (2021). High-resolution imaging of the M_L 2.9 August 2019 earthquake in Lancashire, United Kingdom, induced by hydraulic fracturing during Preston New Road PNR-2 operations, *Seismol. Res. Lett.* **92,** 151–169.

Kettlety, T., J. P. Verdon, M. Werner, and J.-M. Kendall (2020). Stress transfer from opening hydraulic fractures controls the distribution of induced seismicity, *J. Geophys. Res.* **125,** e2019JB018794, doi: 10.1029/2019JB018794.

Kong, Q., D. T. Trugman, Z. Ross, M. J. Bianco, B. J. Meade, and P. Gerstoft (2019). Machine learning in seismology: Turning data into insights, *Seismol. Res. Lett.* **90,** 3–14.

Li, J., J. Rojas-Parra, R. O. Salvage, D. W. Eaton, K. A. Innanen, Y. J. Gu, and W. Sun (2024). Machine learning aids rapid assessment of aftershocks: Application to the 2022-2023 Peace River earthquake sequence, Alberta, Canada, *Seism. Record* **4,** 21–31.

Lund Snee, J.-E., and M. D. Zoback (2020). Multiscale variations of the crustal stress field throughout North America, *Nat. Commun.* **11,** 1951.

Mendoza, C., and S. H. Hartzell (1988). Aftershock patterns and main shock faulting, *Bull. Seismol. Soc. Am.* **78,** 1438–1449.

Mousavi, S. M., W. L. Ellsworth, W. Zhu, L. Y. Chuang, and G. C. Beroza (2020). Earthquake transformer—An attentive deep-learning model for simultaneous earthquake detection and phase picking, *Nat. Commun.* **11,** 3952.

Nantanoi, S., G. Rodríguez-Pradilla, and J. P. Verdon (2022). 3D-seismic interpretation and fault slip potential analysis from hydraulic fracturing in the Bowland Shale, UK, *Pet. Geosci.* **28,** petgeo2021-057, doi: 10.1144/petgeo2021-057.

Oprsal, I., and L. Eisner (2014). Cross-correlation—An objective tool to indicate induced seismicity, *Geophys. J. Int.* **196,** 1536–1543.

Park, Y., G. C. Beroza, and W. L. Ellsworth (2022). Basement fault activation before larger earthquakes in Oklahoma and Kansas, *Seism. Record* **2,** 197–206.

Peña-Castro, A. F., M. P. Roth, A. Verdecchia, J. Onwuemeka, Y. Liu, R. M. Harrington, Y. Zhang, and H. Kao (2020). Stress chatter via fluid flow and fault slip in a hydraulic fracturing induced earthquake sequence in the Montney formation, British Columbia, *Geophys. Res. Lett.* **47,** e2020GL087254, doi: 10.1029/2020GL087254.

Podvin, P., and I. Lecomte (1991). Finite difference computation of travel times in very contrasted velocity models: A massively parallel approach and its associated tools, *Geophys. J. Int.* **105,** 271–284.

Roth, M. P., K. B. Kemna, R. M. Harrington, and Y. Liu (2022). Source properties of hydraulic-fracturing-induced earthquakes in the Kiskatinaw area, British Columbia, Canada: *J. Geophys. Res.* **127,** e2021JB022750, doi: 10.1029/2021JB022750.

Salvage, R. O., D. W. Eaton, C. M. Furlong, J. Dettmer, and P. K. Pedersen (2024). Induced or natural? Toward rapid expert assessment, with application to the MW 5.2 Peace River earthquake sequence, *Seismol. Res. Lett.* **95,** 758–772.

Samaroo, M., R. Chalaturnyk, and M. Dusseault (2023). Estimating sustainable long-term fluid disposal rates in the Alberta Basin, *Energies* **16,** 2532.

Sambridge, M. (1999). Geophysical inversion with a neighbourhood algorithm—I. Searching a parameter space, *Geophys. J. Int.* **138,** 479–494.

Schultz, R., and V. Stern (2015). The Regional Alberta Observatory for Earthquake Studies Network (RAVEN), *Canadian Society of Exploration Geophysicists Recorder*, Vol. 40, 34–37.

Schultz, R., and L. Telesca (2018). The cross-correlation and reshuffling tests in discerning induced seismicity, *Pure Appl. Geophys.* **175,** 3395–3401.

Schultz, R., and R. Wang (2020). Newly emerging cases of hydraulic fracturing induced seismicity in the Duvernay East Shale Basin, *Tectonophysics* **779,** 228393, doi: 10.1016/j.tecto.2020.228393.

Schultz, R., J.-U. Woo, K. Pepin, W. L. Ellsworth, H. Zebkar, P. Segall, Y. J. Gu, and S. Samsonov (2023). Disposal from in situ bitumen recovery induced the M_L 5.6 Peace River earthquake, *Geophys. Res. Lett.* **50,** e2023GL102940, doi: 10.1029/2023GL102940.

Schultz, R., V. Stern, and Y. J. Gu (2014). An investigation of seismicity clustered near the Cordel Field, west central Alberta, and its relation to a nearby disposal well, *J. Geophys. Res.* **119,** 3410–3423.

Vasyura-Bathke, H., J. Dettmer, K. Biegel, R. O. Salvage, D. Eaton, N. Ackerley, S. Samsonov, and T. Dahm (2023). Bayesian inference elucidates fault-system anatomy and resurgent earthquakes induced by continuing saltwater disposal, *Commun. Earth Environ.* **4,** 407.

Verdecchia, A., E. S. Cochran, and R. M. Harrington (2021). Fluid-earthquake and earthquake-earthquake interactions in southern Kansas, USA, *J. Geophys. Res.* **126,** e2020JB020384, doi: 10.1029/2020JB020384.

Verdon, J. P. (2014). Significance for secure CO_2 storage of earthquakes induced by fluid injection, *Environ. Res. Lett.* **9,** 064022, doi: 10.1088/1748-9326/9/6/064022.

Verdon, J. P., B. J. Baptie, and J. J. Bommer (2019). An improved framework for discriminating seismicity induced by industrial activities from natural earthquakes, *Seismol. Res. Lett.* **90,** 1592–1611.

Verdon, J. P., J.-M. Kendall, D. J. White, and D. A. Angus (2011). Linking microseismic event observations with geomechanical models to minimise the risks of storing CO_2 in geological formations, *Earth Planet. Sci. Lett.* **305,** 143–152.

Vilarrasa, V., and J. Carrera (2015). Geologic carbon storage is unlikely to trigger large earthquakes and reactivate faults through which CO_2 could leak, *Proc. Natl. Acad. Sci.* **112,** 5938–5943.

Wang, B., H. Kao, H. Yu, R. Visser, and S. Venables (2022). Physical factors controlling the diverse seismogenic behavior of fluid injections in Western Canada, *Earth Planet. Sci. Lett.* **589,** 117555, doi: 10.1016/j.epsl.2022.117555.

Wang, B., H. Kao, H. Yu, R. Visser, and A. Verdecchia (2023). Quantitative evaluation of the competing effects of wastewater disposal and hydraulic fracturing on causing induced earthquakes: A case study of an M 3.1 earthquake sequence in western Canada, *J. Geophys. Res.* **128,** e2022JB025048, doi: 10.1029/2022JB025048.

Wang, B., A. Verdecchia, H. Kao, R. M. Harrington, Y. Liu, and H. Yu (2021). A study on the largest hydraulic fracturing induced earthquake in Canada: Numerical modeling and triggering mechanism, *Bull. Seismol. Soc. Am.* **111,** 1392–1404.

Wang, R., B. Schmandt, M. Zhang, M. Glasgow, E. Kiser, S. Rysanek, and R. Stairs (2020). Injection-induced earthquakes on complex fault zones of the Raton Basin illuminated by machine-learning phase picker and dense nodal array, *Geophys. Res. Lett.* **46,** e2020GL088168, doi: 10.1029/2020GL088168.

Weides, S. N., I. S. Moeck, D. R. Schmitt, and J. A. Majorowicz (2014). An integrative geothermal resource assessment study for the siliciclastic Granite Wash Unit, northwestern Alberta (Canada), *Environ. Earth Sci.* **72,** 4141–4154.

Yenier, E. (2017). A local magnitude relation for earthquakes in the Western Canada Sedimentary Basin, *Bull. Seismol. Soc. Am.* **107,** 1421–1431.

Zhu, W., and G. C. Beroza (2019). PhaseNet: a deep-neural-network-based seismic arrival-time picking method, *Geophys. J. Int.* **216,** 261–273.

Manuscript received 24 April 2025
Published online 10 July 2026